Research Article

Synthesis, plasmonic properties, and CWA simulant decontamination activity of first row early transition metal nitride powders and nanomaterials

Andrew P. Purdy[1] · Olga A. Baturina[1] · Blake S. Simpkins[1] · Spencer Giles[1] · Todd Brintlinger[2] · James Wynne[1]

Abstract
The complexes $MCl_3(THF)_3$ (M = Ti, V, Cr) were used as precursors to form early transition metal nitrides, and solid solutions of these isomorphous complexes $M_xM'_{1-x}Cl_3(THF)_3$ were prepared by co-crystallization. Heating the precursor under NH_3 flow from 800 to 950 °C produced powders of the nitride MN, and solid solutions of these precursors produced alloys of the nitrides. Nanomaterials were synthesized by two methods: (1) reaction of a $MCl_3(THF)_3$ solution with 3 eq of KNH_2 in THF in the presence (or absence) of oleylamine, followed by nitridation under NH_3 flow at 650–950 °C and (2) loading a porous catalyst support such as pelletized Al_2O_3 with the $MCl_3(THF)_3$ complex, followed by similar heat treatment. The materials were characterized by powder X-ray diffraction, elemental analysis, SEM, and optical spectroscopy. Diffuse reflectance and UV–Vis-NIR spectroscopy showed the local surface plasmonic resonances (LSPRs). Although diffuse reflectance and UV–Vis-NIR spectroscopy showed LSPRs whose position was sensitive to surface functionalization and conditions of preparation, preliminary results show TiN nanoparticles have some activity in the degradation of the Chemical Warfare Agent (CWA) simulant DEMETON-S, but light plays no role in the mechanism.

Keywords Titanium nitride · Plasmon · Solid solutions,·nanomaterials,·demeton-S · Refractory plasmonics

1 Introduction

Some early transition metal nitrides, particularly TiN and ZrN, have optical properties similar to noble metals (e.g., Au, Ag), making them potential drop-in replacements for these expensive and, in some cases, chemically unstable materials. In fact, TiN has been shown to exhibit plasmonic resonances similar to those of Au but at a far reduced cost and with much greater thermal stability [1–7]. Additionally, there is already a fair body of literature that already describes the use of hot charge carriers, generated via plasmon decay [8], to perform a number of reactions [9], including water oxidation [10, 11], water reduction [12–14], oxidation of amines to aldehydes [15], CO_2 reduction [16], and NH_3 decomposition [17]. Typically, these demonstrations have utilized Au plasmonic nanoparticles on a semiconducting support, [18] often TiO_2 [19]. These metal–semiconductor heterosystems may serve to enhance charge separation as well as promote the reaction of interest if a catalytic semiconductor is used. In the

present work,[1] we prepared nanomaterials of the first row early transition metal nitrides, and their solid solutions, and tested select variants for activity in degradation of the Chemical Warfare Agent (CWA) simulant Demeton-S. We are operating under the presumption that a thin layer of TiO_2 is present on all TiN particles that have been exposed to air, and this will be the surface upon which reactions occur.

2 Experimental

2.1 General comments

All solvents for organometallic synthesis were dried from either sodium (toluene), sodium benzophenone ketyl (THF) or P_2O_5 (CH_2Cl_2) and distilled before use. Solvents for Demeton-S experiments were not dried. All manipulations of anhydrous metal chlorides and organometallic complexes were done under inert atmosphere (argon) in a recirculating dry box or under N_2 in a flow box, but once converted to metal nitrides, the products were handled in air. KNH_2 was made from a reaction between K and NH_3 in a stainless steel cylinder. Powder XRD patterns were recorded on a Rigaku SmartLab 2080B212 3 kW powder X-ray diffractometer with Cu Kα radiation, and BET measurements were obtained on an Micromeritics ASAP 2020. Visible light absorption of synthesized nanoparticles, and γ-Al_2O_3 supported TiN and Au powders were characterized by UV–Vis spectra, which were collected on water or methanol dispersions in transmission mode, and in diffuse reflectance mode for powdered samples, using a Perkin-Elmer UV/VIS/NIR λ 1050 spectrometer. Powdered samples were diluted to 3 wt% with KBr prior to collecting diffuse reflectance spectra, and an integrated sphere was used. X-ray photoelectron spectroscopy (XPS) was done on a Thermo-Fisher Nexsa instrument.

2.2 Synthesis of $MCl_3[THF]_3$

Complexes were prepared in a similar manner to [20–22]. (a) M = Ti 50 mL THF was slowly added to 10 g $TiCl_3(AlCl_3)_{1/3}$ (Aldrich) in 150 mL toluene in the dry box and stirred until fully reacted, and mixture was heated to dissolve. When the mixture had cooled, it was filtered and the blue crystals were washed with more a toluene-THF mixture and

a small amount of THF and pumped dry, affording 17.3 g $TiCl_3(THF)_3$ (93%). (b) VCl_3 (10.79 g) was mixed with 150 mL THF and heated at 70 °C for 3 days. Toluene added at room temperature and pink crystals were isolated by filtration and pumped dry. 22.81 g (89%) isolated. (c) Anhydrous $CrCl_3$ (7.5 g, 47.3 mmol) was mixed with 50 mL THF, 20 mL CH_2Cl_2, and a pinch of Zn dust and was agitated in the flow box until the exotherm had subsided, and then was sonicated for 15 min and filtered in the flow box. The filtrate was pumped to dryness, affording 15.166 g (86%) $CrCl_3(THF)_3$. (d) Except for **A5,** mixed solid solutions were prepared by combining portions of the individual metal complexes in CH_2Cl_2, and allowing the solution to slowly evaporate in the N_2 flow box to afford crystals of mixtures. The precursor for **A5** was made by dissolving the Ti and V salts in hot THF and allowing to cool.

2.3 Preparation of nanoparticle precursors

Three different types of precursors were used for MN nanoparticles, and the specific conditions for each sample are listed in Table 1. All materials with the exception of the final product were handled under inert atmosphere. On all cases, the final product was washed with water to remove salts and with ethanol and dried. For the (**A**) samples, the $MCl_3(THF)_3$ complex (either single metal or mixtures prepared as described above) was directly placed in an Al_2O_3 boat inside a tube furnace. In one instance, a quartz slide was placed near the boat and a film of VN was deposited on the slide, in addition to the powders. (**B**) $TiCl_3(THF)_3$ (1.01 g, 2.72 mmol) was mixed with KNH_2 (0.465 g, 8.43 mmol) in about 30 mL of THF in a bulb with a Kontes teflon valve. The bulb was sonicated overnight and the solvent pumped off, affording 0.827 g precursor. A ~ 50% portion of this solid was placed in an Al_2O_3 boat in a tube furnace and heated as described below. After washing with water and drying, 106 mg TiN (**B1**) was isolated. (C) $MCl_3(THF)_3$ was mixed with KNH_2 and oleylamine in ~ 40 mL THF, with the amounts used in each case listed in Table 1. The bulb was sonicated for several hours, heated overnight at 80 °C, and filtered in drybox. The black precursor powder was loaded into the Al_2O_3 boat and heated as described below.

2.4 Conversion of precursor into nanomaterials, series A, B, C

The precursor was loaded into an alumina boat, which was inserted into a quartz tube under inert atmosphere. The tube was placed in a tube furnace under flowing NH_3, the temperature was first increased to an intermediate temperature of 200–250 °C for about 1 h, then a higher intermediate temperature of 350–450 °C for about an hour

Table 1 Synthesis conditions and results for MN nanomaterials

	Intermediate temps (°C)	Final temp (°C, time)	Yield (g)	BET (m^2/g)	XRD (phase; crystallite size*)
Method A					
Precursor [MCl$_3$(THF)$_3$] (g)					
A1 Ti (0.54)	250, 400, 650 °C	850 16 h	0.074 (82%)	20.73	TiN; 30 nm
A2 V (2.04)	200, 450	900 1 h	0.34 (96%)	7.16	VN; 42 nm
A3 V (0.76)	200. 450	900 2 h	0.13 (98%)	0.29***	VN; 60 nm
A4 Cr (1.035)	250, 450	850 2 h	0.17 (93%)	0.33***	CrN; 60 nm, Cr$_2$N; 53 nm
A5 Ti-V (1.34)	250, 450	850 1 h	0.19 (83%)	34.42	MN; 15 nm
A6 Ti-Cr (0.99)	200, 450	850 2 h	0.12 (71%)	0.67 ***	MN; 19 nm, M$_2$N
A7 Ti-V-Cr (1.50)	200, 450	850 2 h	0.22 (85%)	7.67	MN; 25 nm
Method B					
[TiCl$_3$(THF)$_3$], KNH$_2$					
B1 1.01 g, 0.465 g KNH$_2$	150, 250	850 °C 16 h	0.106 (50% of precursor)	45.40	TiN; 15 nm
Method C					
MCl$_3$(THF)$_3$; KNH$_2$; OA(g)					
C1 M = Ti 2.02; 0.92; 1.01	200, 350	850 1 h	0.17 ~ 50% portion	201.72	TiN; 6 nm
C1a	200	650 1 h	0.18 ~ 50% portion	183.55	TiN; 4 nm
C2 (Ti-V-Cr) Ti 0.74 V 0.77 Cr 0.81 1.03 KNH$_2$; 1.23 g OA	250, 350	850 1 h	0.42	174.53	MN; 6 nm
C3 V 1.99; 0.89; 1.28 OA	250, 350	850 1 h	0.31	101.68	VN; 18 nm
C4 Cr 1.57; 0.70; 1.28 OA	200, 450	850 ½ h	0.25	139.68	CrN; 11 nm, carbides, carbonitrides
C5 Cr 1.24; 0.55; 1.2 OA	250. 350	800 1 h	0.25	57.03	CrN; 19 nm, Cr$_2$O$_3$

OA oleylamine

*Determined by Rigaku PDXL-2 software v 2.0.3.0 using Halder-Wagner method

**Only a 50% portion of precursor used

***Insufficient sample for accurate reading—surface area too low

and then the final temperature of typically 800–900 °C for 1 or more hours. The conditions for each sample are listed in Table 1.

2.5 Impregnation of oxide catalyst support pellets (series D)

(a) Pelletized γ-Al$_2$O$_3$ (Alfa #43,832) was heated under dynamic vacuum at 550 °C until no more gas was evolved, and allowed to cool. In the dry box, 0.993 g dried Al$_2$O$_3$ pellets was mixed with TiCl$_3$(THF)$_3$ (0.751 g) and dry CH$_2$Cl$_2$ was added. After several hours, the solution was decanted and the pellets washed with a small amount of CH$_2$Cl$_2$. The impregnated pellets were pumped dry and then heated in a tube furnace under NH$_3$ flow at 250 °C for 0.5 h, then at 450 °C for 16 h and at 900 °C for 3 h. Total mass of impregnated pellets (**D1**) is 1.075 g (weight gain 7.62%). (b) Dry Al$_2$O$_3$ pellets (0.603 g) was mixed with 1.00 g of HAuCl$_4$ solution (0.1469 M) and let dry at about 50 °C, and heated under H$_2$ flow in tube furnace at 250 °C for 1 h and 500 °C for 2 h, affording purplish colored pellets (**D2**) with mass 0.6181 g (weight gain 2.44%).

2.6 Chemical agent simulant decontamination challenge

Synthesized titanium nitride (**C1**) and titanium nitride impregnated in γ-alumina (**D1**) were challenged with CWA simulant Demeton-S (S-(2-Ethylthioethyl) O,O-dimethyl phosphorothioate). Demeton-S was deposited onto these substrates from a stock solution composed of 10.5 µL (4.66 × 10^{-5} mol) Demeton-S in 2 mL of methylene

Table 2 Mass of individual catalysts challenged with Demeton-S

Catalyst	0 h Exposure (mg)	6 h exposure (mg)	24 h exposure (mg)
Control-1	0	0	0
Control-2	0	0	0
TiN-1	1.67	1.28	1.13
TiN-2	0.83	1.13	0.96
TiN-Al$_2$O$_3$-1	1.48	1.10	1.90
TiN-Al$_2$O$_3$-2	2.32	1.40	1.30

Method A, B -- Lower Surface Area Powders

Fig. 1 X-ray powder patterns of the A and B series metal nitride materials. JCPDS reference patterns for TiN and VN indicated

chloride (CH$_2$Cl$_2$). Depositions consisted of 20 µL of the stock solution deposited onto the solid substrates of various masses (Table 2) contained in a 200 µL GC clear glass vial inserts contained within a standard 2 mL GC vial. After deposition the methylene chloride was allowed to evaporate (1 h) depositing the Demeton-S onto the surface of the nanoparticles. After solvent evaporation the GC vials were sealed and then extracted at various time intervals after the solvent evaporation was performed: immediately (0 h), after 6 h and after 24 h. Additional control depositions were also performed into empty vial inserts and extracted at the same time intervals following the same protocol. Two extractions were performed with acetonitrile (MeCN) in which 100 µL of MeCN was deposited onto the nanoparticles and allowed to extract the organic products and transferred to new 2 mL GC vials. Following the extractions 800 µL of MeCN was added to the GC vial to dilute to 1000 µL (1 mL) prior to analysis.

Analysis for the percent reduction of Demeton-S and byproducts was performed using GC–MS. GC–MS analysis was performed using an Agilent 7890B gas chromatograph coupled with an Agilent 5977 B mass spectrometer operating in electron ionization (EI) mode and an Agilent 7693 autosampler (Agilent Technologies, Santa Clara, CA, USA). The GC–MS was equipped with a Restek 5HT capillary column (Restek Corporation, Bellefonte, PA, USA) operating in split injection mode with a split ratio of 5:1 for 1 µL injection volumes with helium carrier gas at a flow of 1.2 mL/min. The temperature program for the GC–MS had an initial temperature of 100 °C for 1 min then the temperature was ramped at 20 °C/min to 130 °C followed by a 15 °C/min ramp up to 285 °C with a post run hold of 300 °C for 2.5 min. The injection temperature, MS quad temperature, and source temperature were 275, 150, 230 °C, respectively. The solvent delay was set to 1.75 min and the MS detector was set to scan from 34 to 350 m/z. The percent reduction for each challenge was calculated from the concentration of the Demeton-S deposited and the measured concentration from the samples and the controls. The concentration of Demeton-S for each challenge
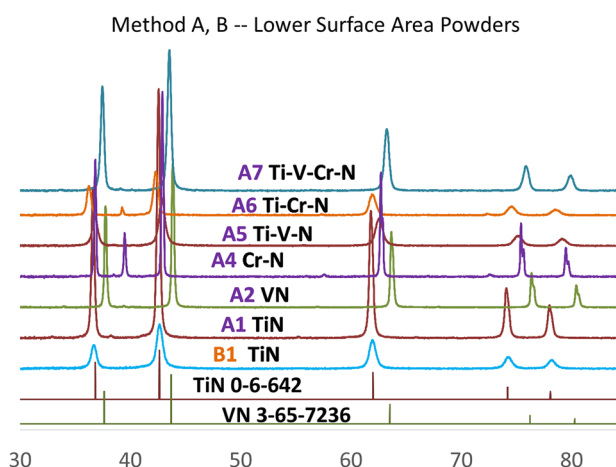
and control was calculated using a calibration curve generated from known concentrations of Demeton-S (SI).

3 Results and discussion

3.1 Material synthesis and characterization

The early transition metal trichloride tris-THF adducts [MCl$_3$(THF)$_3$] [M = Ti, V, Cr] are excellent precursors to bulk nanostructured metal nitrides MN, simply by heating the precursor material in a tube furnace under flowing, anhydrous ammonia. Since the precursor has almost no vapor pressure, most of the produced nitride remains in the alumina boat in which the precursor was placed, and the yields range from 71 to 98%. With the Ti and V precursors, films that are presumably metal nitride did deposit on the quartz tube and the alumina boat containing the precursor. As a test of film growth, in one instance (**A3**), a quartz slide was placed with the boat and a film of VN was deposited on the slide. All of the nitride products are single phase except with Cr, where some powder XRD peaks for Cr$_2$N were evident (Fig. 1). Additionally, all of the trichloride precursors have similar crystal structures and solubilities in CH$_2$Cl$_2$, and crystals of mixed precursors were easily prepared by slowly evaporating a CH$_2$Cl$_2$ solution of the precursors under inert atmosphere conditions. Those crystals were converted into nitrides in the same manner, and produced single phase MN as determined by XRD, except in the case of **A6**, which had a high fraction of Cr. The XRD patterns are shown in Fig. 1. Typically, the line widths of materials produced from a single metal were much narrower than those produced from a mixture of metals, indicating larger crystallite sizes in the single metal cases. However, the morphology of the metal nitrides
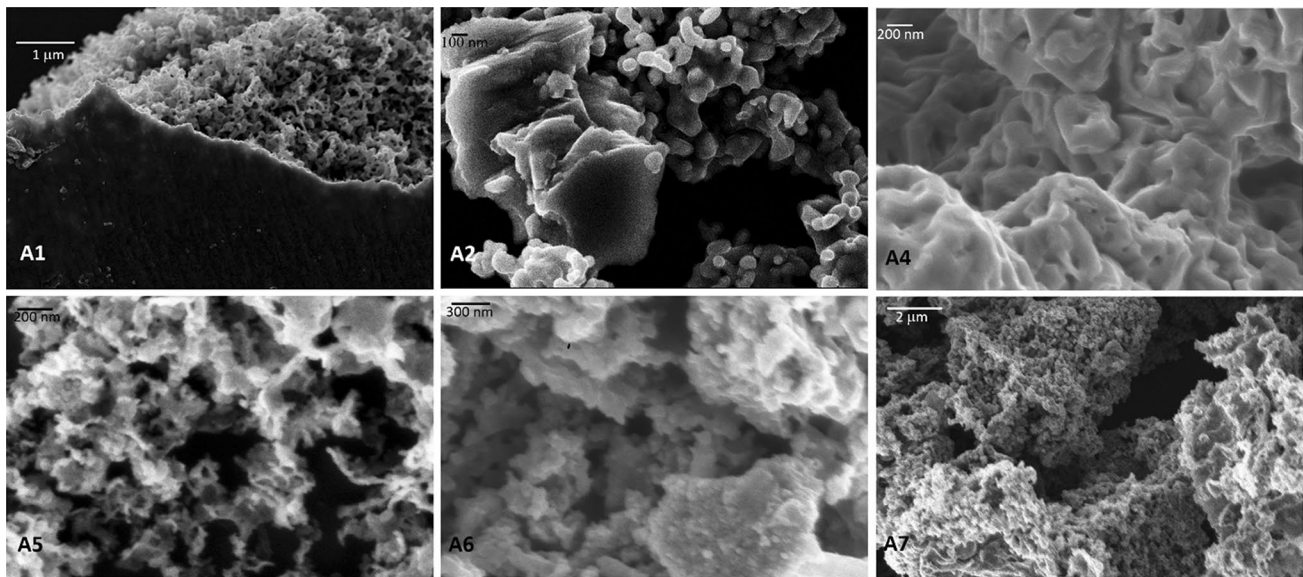
Fig. 2 SEM images of representative MN materials obtained by thermolysis of $MCl_3(THF)_3$ under flowing ammonia

produced in this manner was typically a porous network composed of nanoparticles fused together, as evidenced by the SEM images (Fig. 2). BET data (Table 1) shows higher surface areas that correlate to lower thermolysis temperatures and shorter heating times, as expected. The difference between **A2** and **A3** is quite illustrative. Here, thermolysis at 900 °C for 2 h instead of 1 h produced VN with a much lower surface area, as the sintering of the grains is very time dependent, and the crystallite sizes increased modestly. The XPS data on **A3** also shows probable nitrogen loss. Also, TiN is more refractory than VN and CrN, and the BET data is consistent with this.

Since the goal was to generate individual nanoparticles and not macroscopic, albeit porous, materials, the synthesis was modified. Reaction of the $TiCl_3(THF)_3$ precursor with 3 eq of KNH_2 prior to thermolysis also produced porous materials composed of nanoparticles (**B1**), but adding oleylamine to that reaction (series **C**) accomplished the goal of producing individual nanoparticles that were only moderately agglomerated. BET surface areas were high, ranging from 57 to 202 m^2/g, and the particle size calculated from BET was mostly consistent with the crystallite sizes determined by XRD, of which the powder patterns are shown in Fig. 3. While the preparations involving just Ti–N (**C1**), V–N (**C3**), and the mixture Ti–V–Cr–N (**C2**) showed just broad lines for the nitrides in their XRD patterns, the preparation of Cr–N which was heated to intermediate temperatures of 200 and 450 °C (**C4**) showed evidence for carbides and carbonitrides, as well as chromium oxide. Apparently, carbonization occurred before the organics were thoroughly baked out. A repeat that was heated to intermediate temperatures of 250 and 350 °C

(**C5**) lacked any peaks for those carbides or carbonitrides, but still showed the presence of Cr_2O_3. The origin of the oxygen in these products is unclear.

In order to maximize the light absorption of small TiN nanoparticles by avoiding their agglomeration and oxidation, they were in-situ deposited on a porous support. Gold nanoparticles were deposited in the same manner to serve as a reference (series **D** nanomaterials). We used a nonreactive support, porous γ-alumina, due to the complications presented by porous TiO_2 (which is commercially available), but is reactive under a stream of flowing NH_3 and presents issues that will not be discussed here. In these examples, the TiN was loaded into the support at about a 7 wt% concentration which
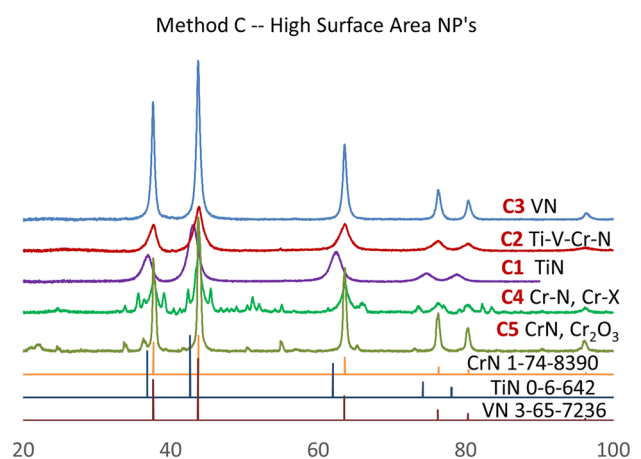

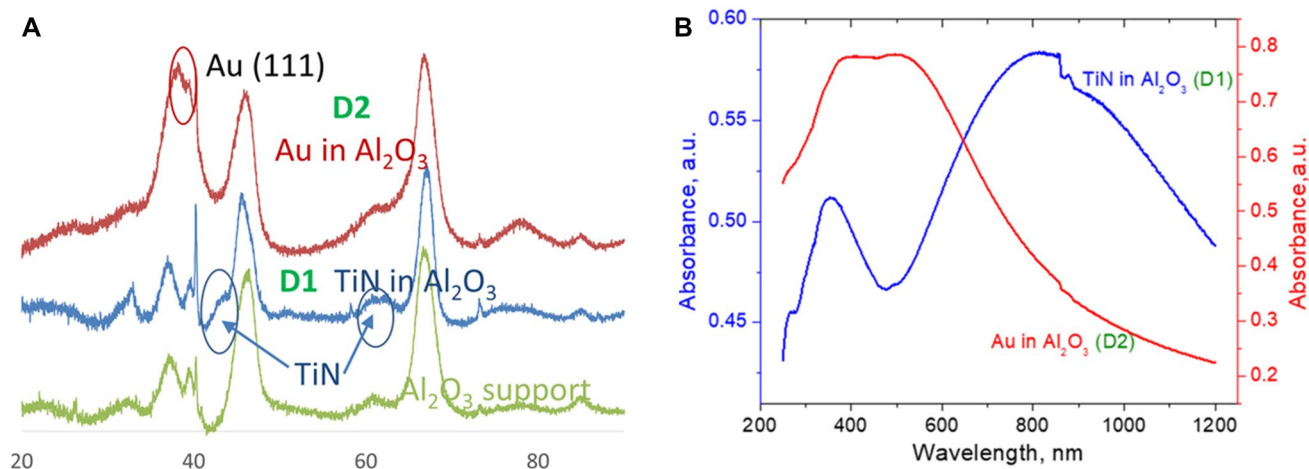**Fig. 3** XRD powder patterns of high surface area nanopowders, series C

Fig. 4 **a** XRD powder patterns of the **D** series materials and the pure Al_2O_3 support for comparison. **b** Kubelka-Monk transformations of diffuse reflectance spectra of the **D** series materials recorded on KBr mixtures using an integrating sphere

represented the maximum amount of $TiCl_3(THF)_3$ precursor that could be absorbed into the support. For the case of Au, the 2% loading achieved here is probably nowhere near the maximum achievable, since the concentration of the stock $HAuCl_4$ solution used was fairly low. While the XRD powder pattern of these materials shows evidence for the most prominent peaks of Au and TiN (Fig. 4a), those peaks are heavily obscured by reflections from the support and are not conclusive. Therefore we performed transmission electron microscopy (TEM) on these materials, which clearly show crystals of Au and TiN present due to morphology differences as well as intensity contrast, as seen in Fig. 5. These images show 3–4 nm cubic TiN and 20–30 nm spherical Au crystals. The small TiN nanocrystals are not agglomerated and evenly dispersed in the support.

All of the materials were analyzed by XPS for elemental composition, which is tabulated in the supporting information. For all materials, there is considerable oxygen and carbon on the surface, even in the **A** series, where the amount of carbon in the bulk should be much less, from stoichiometry and mass balance (yield) concerns alone. This is attributed to the fact that XPS is a surface, not a bulk, technique, and adventitious carbon and oxygen are present on nearly all materials. The cubic TiN crystal structure can be non-stoichiometric and can accommodate considerable substitution of nitrogen by carbon and oxygen, so the metal nitrogen ratios should be a better indicator of composition. These M:N ratios for the **A** series are close to 1 except for **A3** (V:N 1.89), which could be nitrogen deficient because it was heated for 2 h instead of 1 h, and **A5** (M:N 1.35) which also contains V and is nitrogen deficient. **A1** and **A5** contain potassium, which was not present in the starting materials

and is thus attributed to surface contamination from the alumina boat or the quartz tube in which the reaction was done (as the reactions that did contain potassium were actually done before these two). The **C** series is all nitrogen deficient, and this is as expected since a lot of carbon is present in oleylamine. Residual potassium is present in most of the **C** series. In cases where multiple metals are present, the ratios approximately reflect the ratios of starting materials, except for **A7**, which is vanadium deficient. Apparently, when a solution of the Ti, V, and Cr salts crystallized from CH_2Cl_2, more of the $VCl_3[THF]_3$ remained in solution.

3.2 Optical properties of materials

Comparison of UV–Vis spectra displayed in Fig. 6 shows that our coarser VN (**A2**) and Ti–V–N (**A5**) nanoparticles dispersed in water exhibit a broad absorption maxima centered around 800 nm. TiN (**C1**) nanoparticles dispersed in H_2O demonstrate two rising branches extending to the left and right from 650 nm, with no clearly pronounced absorption maximum. On the contrary, **C1** particles dispersed in CH_3OH demonstrate a clearly pronounced LSPR at ~ 900 nm. The absence of LSPR in water is likely due to oxidation and agglomeration of the ca 6 nm TiN nanoparticles. The strongest LSPR is observed for aqueous suspensions of 30 nm commercial TiN nanoparticles (Fig. 6b, green curve). The maximum centered at 700 nm is blue-shifted vs. those of **C1** TiN NPs in CH_3OH, and VN and Ti–V–N in H_2O. The red-shift and broadening of plasmonic resonances of 6 nm TiN, and 15 nm Ti–V–N NPs vs 30 nm TiN NPs is likely due to their stronger oxidation [23]. Diffuse reflectance spectra measured on TiN/γ-Al_2O_3 and Au/γ-Al_2O_3 powders
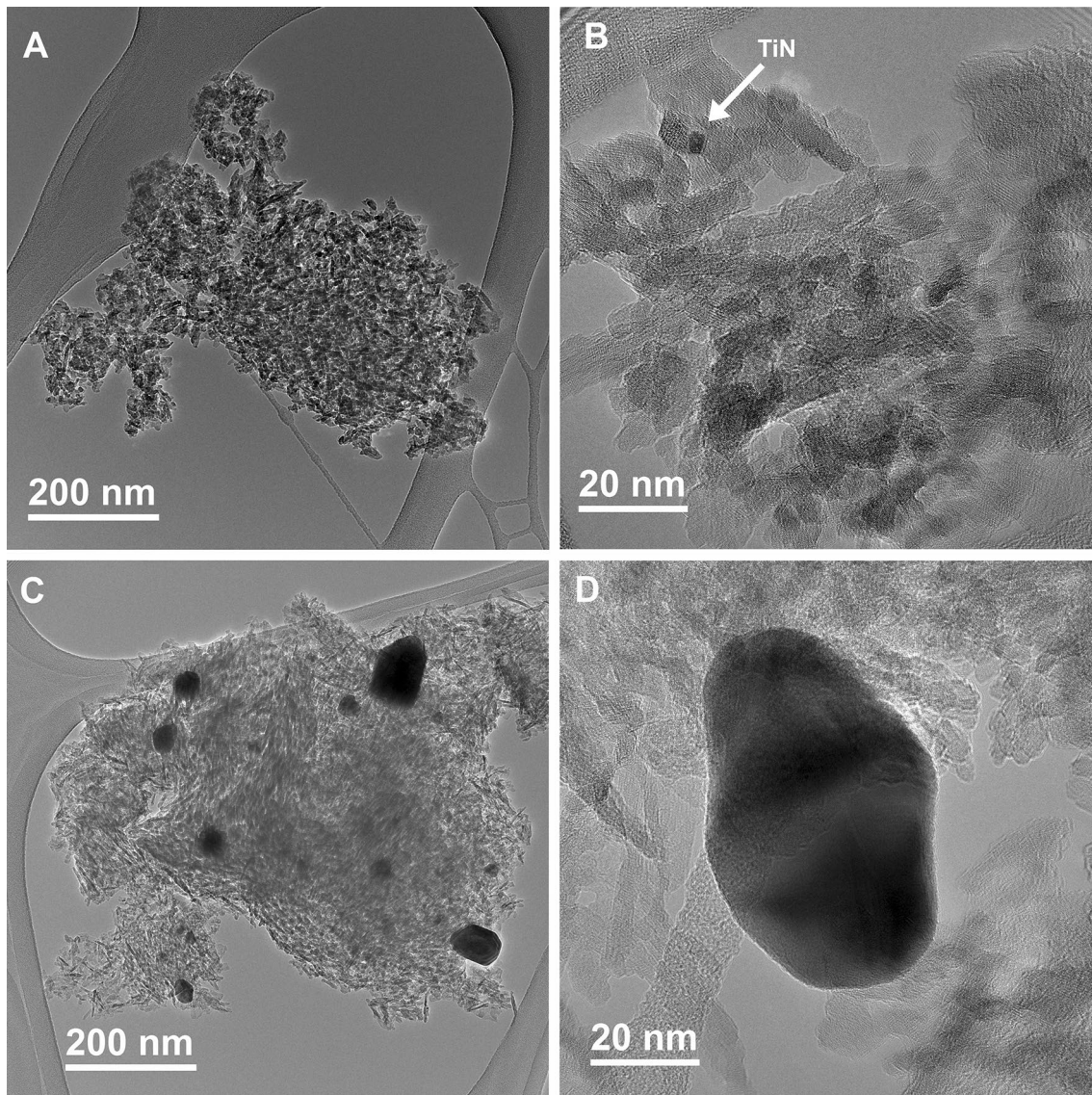
Fig. 5 TEM bright-field images of **D1** (TiN/γ-Al$_2$O$_3$, A, B) and **D2** (Au/γ-Al$_2$O$_3$, C, D). Images were obtained in a JEM2200FS TEM operating at 200 keV with a One View electron camera

are depicted in Fig. 4b. A clearly pronounced absorption maximum at ~ 800 nm is observed for TiN/γ-Al$_2$O$_3$ (**D1**). The maximum is ~ 100 nm blue-shifted compared to its solution counterpart, probably due to the less pronounced agglomeration/oxidation of TiN nanoparticles, While less pronounced agglomeration of supported TiN nanoparticles is evident from Fig. 5, (**D1**), their less pronounced oxidation can be confirmed by comparison of corresponding Ti2p and N1s XPS spectra (SI). The least oxidized TiN nanoparticles are 30 nm commercial nanoparticles. For Au/ γ-Al$_2$O$_3$ (**D2**), a broad maximum centered at 500 nm is observed. A close examinations shows two overlapping maxima centered at ~ 520 and 390 nm. The first maximum is due to Au LSPR [1], while

the second one is likely due to light absorption by the support.

Although a film-type morphology (produced in reaction **A3** along with powder) is less useful for catalytic decomposition applications, which motivate our work, they do allow for direct measurement of the optical properties. These measurements will allow for prediction of plasmonic resonances and inform subsequent materials design and interrogation. The VN material produced a particularly well-behaved film suitable for ellipsometric measurement of optical properties. This material is metallic in some spectral regions and supports broad plasmonic resonances. We include the measured optical constants of our in-house synthesized VN, along with comparison to
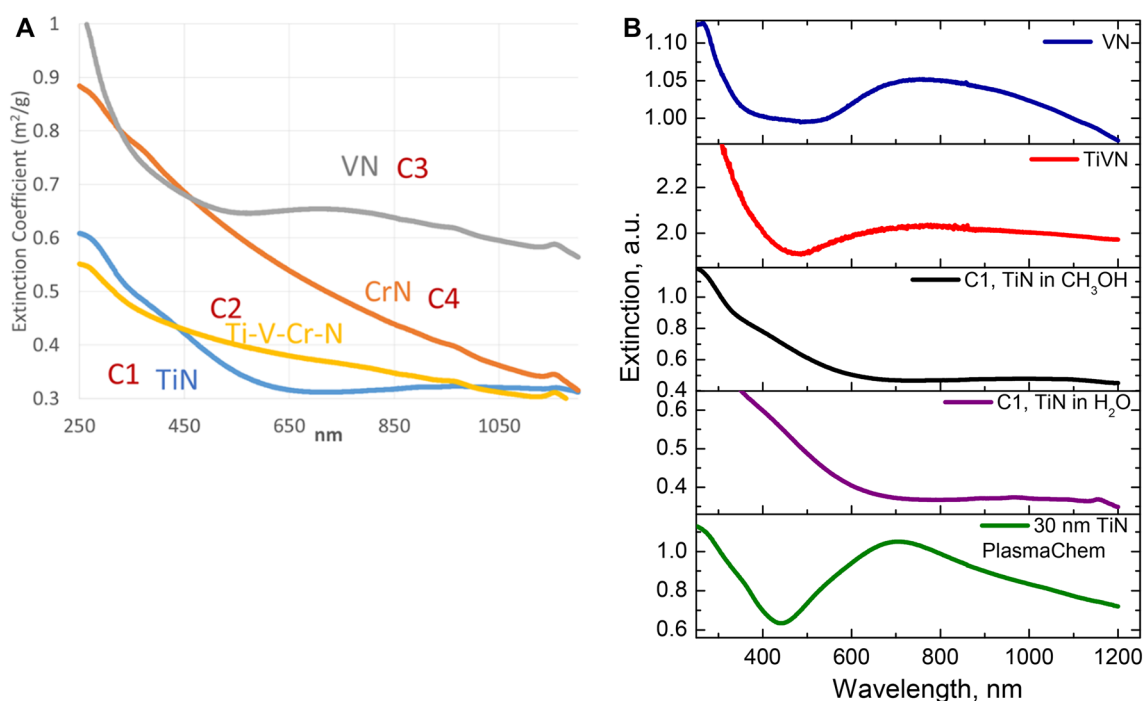
Fig. 6 **a** UV–Vis spectra of dispersions of C series nanomaterials in water. **b** A comparison of various nanomaterials in water and methanol with commercially available TiN nanoparticles (sold as 50 nm, actual size 30 nm) in water and methanol

Fig. 7 Chemical agent simulant Demeton-S (**b**) has both the P-S linkage similar to nerve agent VX (**a**) and the thioether linkage similar to vesicant HD (**c**)
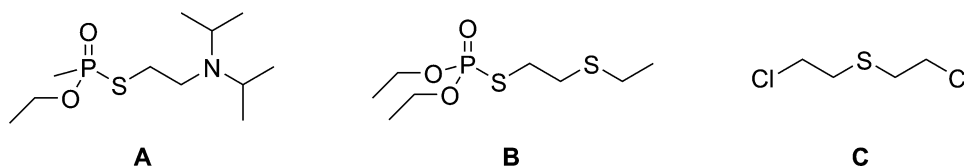
two other literature examples, as well as predicted absorption spectra for this material in the SI. The VN made in this work is comparable to data from the literature [24, 25] and shows a smaller value for the refractive index, *n*. We believe this is most likely due to some porosity of the material, which cause the measured value of *n* to be between that of fully dense VN and of air. Additionally, while the material loss, k, is comparable to the literature examples, it does become more absorptive at wavelengths above ~ 750 nm. These optical properties suggest that our VN should support optical resonances that, for a variety of aspect ratios, could span most of the visible spectrum (see SI). Assuming some distribution in particle aspect ratio, the measured extinction spectra in Fig. 6 are consistent with the optical measured by ellipsometry. We did not grow films of TiN by this method because TiN films have been sufficiently well studied, and the properties of our VN film was very consistent with previous reports.

3.3 Chemical agent simulant decontamination challenge

Demeton-S shown in Fig. 7b is utilized as a simple CWA simulant with the potential to investigate the reactivity of new active materials for decontamination [26–28]. Hydrolysis and oxidation relevant for organophosphate nerve agent VX (Fig. 7a) and/or vesicant sulfur mustard HD (Fig. 7c) can be investigated due to the presence of both a P-S bond and the thioether linkage in Demeton-S [29–34]. In addition to overall percent reduction of the simulant Demeton-S the analysis for and the identification of byproducts was also performed for understanding the chemical reactivity of these materials.

Preliminary screening experiments showed the TiN with the smallest nanoparticle sizes and highest surface area (**C1**) and the TiN impregnated in alumina (**D1**) to be the best materials to test for activity against Demeton-S. Percent reductions for the simulant challenges normalized to the mass of TiN and TiN-Al_2O_3 in addition to control

Table 3 Percent reduction of Demeton-S normalized to catalyst mass with respect to amount of simulant deposited

% Reduction from concentration of simulant deposited[a]	0 h exposure (%)	6 h exposure (%)	24 h exposure (%)
Control-1	5.4	4.4	7.8
Control-2	5.3	17.6*	6.9
TiN-1 (**C1**)	26.9	56.7	56.3
TiN-2 (**C1**)	33.4	53.0	59.3
TiN-Al$_2$O$_3$-1 (**D1**)	25.3	38.6	38.6
TiN-Al$_2$O$_3$-2 (**D1**)	16.0	37.0	42.4

*Extraction inconsistent with others due to glass vial insert taper and enhanced capillary action resulting in an inconsistent extraction compared with other samples

[a]Stock solution prepared 10.5 µL of Demeton-S (4.66×10^{-5} mol) in 2.0 mL CH$_2$Cl$_2$. Deposition of 20 µL stock solution 4.65×10^{-7} mol applied Demeton-S. Catalyst masses presented in Table 2

challenges are shown in Table 3. The control challenges show consistent percent reductions between 4 and 8% indicating minimal loss of simulant during the challenge protocol. Inclusion of the TiN and TiN-Al$_2$O$_3$ into the vial showed significantly improved decontamination performance for all challenge times including the 0 h exposures indicating that some simulant is readily sequestered on to the surface of the materials. Based upon the chromatographs in Fig. 8 and the percent reductions presented in Table 3 the reaction appears to have reached completion within 6 h. The observation of less than 100% reduction is indicative that reactive species on the surface are responsible for the decontamination of Demeton-S which are potentially consumed or blocked after the reaction [30]. This hypothesis is supported by FTIR spectra of KBr pellets of the treated samples which show absorptions
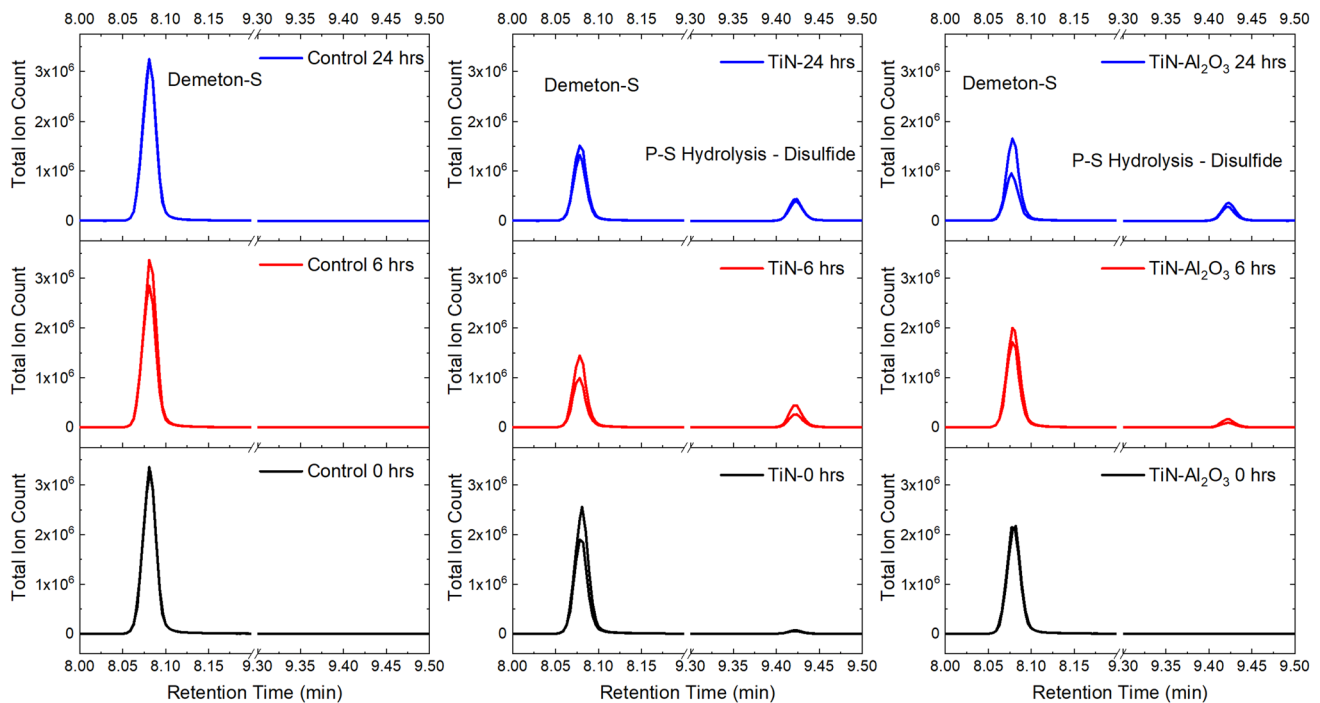

Fig. 8 Chromatograph stacks for control, TiN and TiN-Al$_2$O$_3$ challenges. Each column shows the chromatograms at 0 h(bottom), 6 h (middle) and 24 h (top) for the control (left), TiN sample **C1** (middle) and alumina impregnated TiN sample **D1** (right) at a retention time of 8.08 min (Demeton-S) and the disulfide hydrolysis product at 9.42 min. Each sample was analyzed in duplicate, and the chromatograms are superimposed. Additional data is shown in supporting information
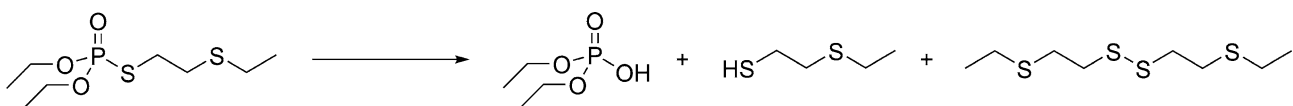

Fig. 9 Demeton-S hydrolysis reaction scheme via cleavage of the P–S bond. The disulfide is believed to form inside the hot inlet of the GC instrument

for phosphate on samples treated with Demeton-S (supporting information). The observed reactivity differences between the two materials challenges is believed to be a result of surface area differences between the two materials. The TiN having a greater surface area has more reactive sites available for hydrolysis of the deposited simulant.

In addition to percent reduction the chromatography results in Fig. 8 show the presence of a byproduct at a retention time of 9.42 min. Analysis of the mass spectrum fragmentation pattern (Supplemental Information) of the byproduct peak indicates hydrolysis of the P–S linkage of Demeton-S to a thiol and subsequent S–S coupling to the disulfide shown in Fig. 9. We believe this S–S coupling is potentially taking place in the inlet of the GC instrument which is kept at 275 °C, as the hydrolysis reaction of organophosphate is consistent with previous reports which conducted analysis on similar materials [30, 35, 36]. The disulfide byproduct is present for both TiN and TiN-Al$_2$O$_3$ materials and is consistent with the preferential reaction route for the decontamination of the organophosphate nerve agent VX with other hydrolytic agents [29–34]. Chromatographs for the TiN-Al$_2$O$_3$ products also show the presence of minor quantities of the thiol hydrolysis product with a retention time of 2.62 min (Fig. S5). The phosphate byproduct was not detected and is believed to be sequestered on the surface of the materials consistent with previous literature reports [30, 35] and our IR measurements on the solids. We do not believe the hydrolysis is catalytic, but is instead a result of active OH groups in the material surface, which are then sequestered by the phosphate.

4 Conclusions

Nanoparticles of TiN, VN, and CrN, and their solid solutions can be prepared effectively from the easily obtained metal trichloride-tri-THF precursors, and nanoparticles can also be easily grown inside a non-reactive support such as porous alumina. Materials made from direct nitridation of the precursor consist of a network of attached nanoparticles, while pre-reaction with KNH$_2$ and oleylamine allows the synthesis of sub 10 nm particles in the bulk. The utilization of synthesized TiN and TiN-Al$_2$O$_3$ show promise toward effective and preferential reactivity toward an organophosphate nerve agent simulant Demeton-S. The reactivity is not dependent on light exposure and thus is not a plasmonic effect. The hydrolysis of the P-S linkage in Demeton-S results in formation and detection of the disulfide and thiol hydrolysis products via GC–MS. Readily synthesized materials with tunable high surface area can find application as a reactive adsorbent material for active decontamination of threats while limiting the generation of hazardous waste from secondary emitters in post contamination scenarios.

Compliance with ethical standards

Conflict of interest The authors declare no conflict of interest.

References

1. Baturina OA, Epshteyn A, Simpkins B, Bhattarai N, Brintlinger TH, Santiago EY, Govorov AO (2019) Comparing photoelectrochemical methanol oxidation mechanisms for gold versus titanium nitride nanoparticles dispersed in TiO$_2$ matrix. J Electrochem Soc 166:H485–H493
2. Guler U, Boltasseva A, Shalaev VM (2014) Refractory plasmonics. Science 344:263–264
3. Guler U, Kildishev AV, Boltasseva A, Shalaev VM (2015) Plasmonics on the slope of enlightenment: the role of transition metal nitrides. Faraday Discuss 178:71
4. Naldoni A, Guler U, Wang ZX, Marelli M, Malara F, Meng XG, Besteiro LV, Govorov AO, Kildishev AV, Boltasseva A, Shalaev VM (2017) Broadband hot-electron collection for solar water splitting with plasmonic titanium nitride. Adv Opt Mater 5:1601031
5. Guler U, Naik GV, Boltasseva A, Shalaev VM, Kildishev AV (2012) Performance analysis of nitride alternative plasmonic materials for localized surface plasmon applications. Appl Phys B 107:285–291
6. Guler U, Ndukaife JC, Naik GV, Nnanna AG, Kildishev AV, Shalaev VM, Boltasseva A (2013) Local heating with lithographically fabricated plasmonic titanium nitride nanoparticles. Nano Lett 13:6078–6083
7. Exarhos S, Alvarez-Barragan A, Aytan E, Balandin AA, Mangolini L (2018) Plasmonic core−shell zirconium nitride−silicon oxynitride nanoparticles. ACS Energy Lett 3:2349–2356
8. Wang F, Melosh NA (2011) Plasmonic energy collection through hot carrier extraction. Nano Lett 11:5426–5430
9. Narang P, Sundararaman R, Atwater HA (2016) Plasmonic hot carrier dynamics in solid-state and chemical systems for energy conversion. Nanophotonics 5:96–111
10. Malara F, Minguzzi A, Marelli M, Morandi S, Psaro R, Dal Santo V, Naldoni A (2015) α-Fe$_2$O$_3$/NiOOH: an effective heterostructure for photoelectrochemical water oxidation. ACS Catal 5:5292–5300
11. Wang S, Gao Y, Miao S, Liu T, Mu L, Li R, Fan F, Li C (2017) Positioning the water oxidation reaction sites in plasmonic photocatalysts. J Am Chem Soc 139:11771–11778
12. DeSario PA, Pietron JJ, Dunkelberger A, Brintlinger TH, Baturina O, Stroud RM, Owrutsky JC, Rolison DR (2017) Plasmonic aerogels as a three-dimensional nanoscale platform for solar fuel photocatalysis. Langmuir 33:9444–9454
13. Li J, Cushing SK, Zheng P, Senty T, Meng F, Bristow AD, Manivannan A, Wu N (2014) Solar Hydrogen generation by a CdS-Au.TiO$_2$ sandwich nanorod array enhanced with Au nanoparticles as electron relay and plasmonic photosensitizer. J Am Chem Soc 136:8438–8449
14. Yan L, Wang F, Meng S (2016) Quantum mode selectivity of plasmon-induced water splitting on gold nanoparticles. ACS Nano 10:5452–5458

15. Sato Y, Naya S, Tada H (2015) A new bimetallic plasmonic photocatalyst consisting of gold(core)-copper(shell) nanoparticle and titanium(IV) oxide support. APL Mater 3:104502

16. DuChene JS, Tagliabue G, Welch AJ, Cheng WH, Atwater HA (2018) Hot hole collection and photoelectrochemical CO_2 reduction with plasmonic Au/p-GaN photocathodes. Nano Lett 18:2545–2550

17. Zhou L et al (2018) Quantifying hot carrier and thermal contributions in plasmonic photocatalysis. Science 362:69–72

18. Knight MW, Sobhani H, Nordlander P, Halas NJ (2011) Photodection with active optical antennas. Science 332:702–704

19. Ahn W, Vurgaftman I, Pietron JJ, Pehrsson PE, Simpkins BS (2019) Energy-tunable photocatalysis by hot carriers generated by surface plasmon polaritons. J Mater Chem A 7:7015–7024

20. Jones NA, Liddle ST, Wilson C, Arnold PL (2007) Titanium(III) Alkoxy-N-heterocyclic Carbenes and a safe, low-cost route to $TiCl_3(THF)_3$. Organometallics 26:755–757

21. Manzer LE (1982) TRICHLOROTRIS(TETRAHYDROFURAN) VANADIUM(III), $VCl_3(THF)_3$. Inorg Synth 21:138

22. Herwig W, Zeiss HH (1958) Chromium trichloride tetrahydrofuranate. J Organic Chem 23:1404

23. Barragan AA, Ilawe NV, Zhong L, Wong BM, Mangolini L, J. (2017) A Non-thermal plasma route to plasmonic TiN nanoparticles. Phys Chem C 121:2316–2322

24. Pflüger J, Fink J, Weber W, Bohnen KP, Crecelius G (1984) Dielectric properties of TiC_x, TiN_x, VC_x, and VN_x from 1.5 to 40 eV determined by electron-energy-loss spectroscopy. Phys Rev B 30:1155–1163

25. Gueddaoui H, Maabed S, Schmerber G, Guemmaz M, Parlebas JC (2007) Structural and optical properties of vanadium and hafnium nitride nanoscale films: effect of stoichiometry. Eur Phys J B 60:305–312

26. Giles SL, Lundin JG, Balow RB, Pehrsson PE, Wynne JH (2017) Comparative roles of Zr^{4+} and Ni^{2+} Wells-Dawson hetero-metal substituted polyoxometalates on oxidation of chemical contaminants. Appl Catal A 542:306–310

27. McGann CL, Daniels GC, Giles SL, Balow RB, Miranda-Zayas JL, Lundin JG, Wynne JH (2018) Air activated self-decontaminating polydicyclopentadiene polyhipe foams for rapid decontamination of chemical warfare agents. Macromol Rapid Commun 39(12):1800194

28. Balow RB, Giles SL, McGann CL, Daniels GC, Lundin JG, Pehrsson PE, Wynne JH (2018) Rapid decontamination of chemical warfare agent simulant with thermally activated porous polymer foams. Ind Eng Chem Res 57(25):8630–8634

29. Roberts G, Maynard RL (2007) Responding to chemical terrorism: operational planning and decontamination. In: Marrs TC, Maynard RL, Sidell FR (eds) Chemical warfare agents: toxicology and treatment, 2nd edn. Wiley, West Sussex, pp 175–190

30. Bandosz TJ, Laskoski M, Mahle J, Mogilevsky G, Peterson GW, Rossin JA, Wagner GW (2012) Reactions of VX, GD, and HD with $Zr(OH)_4$: near instantaneous decontamination of VX. J Phys Chem C 116(21):11606–11614

31. Talmage SS, Munro NB, Watson AP, King JF, Hauschild V (2007) The fate of chemical warfare agents in the environment. In: Marrs TC, Maynard RL, Sidell FR (eds) Chemical warfare agents: toxicology and treatment, 2nd edn. Wiley, West Sussex, pp 89–125

32. Wagner GW, Yang Y (2002) Rapid nucleophilic/oxidative decontamination of chemical warfare agents. Ind Eng Chem Res 41:1925–1928

33. Wagner GW, Sorrick DC, Procell LR, Brickhouse MD, Mcvey IF, Schwartz LI (2007) Decontamination of VX, GD, and HD on a Surface using modified vaporized hydrogen peroxide. Langmuir 23:1178–1186

34. Yang Y, Baker JA, Ward JR (1992) Decontamination of chemical warfare agents. Chem Rev 92:1729–1743

35. Wagner GW, Procell LR, O'Connor RJ, Munavalli S, Carnes CL, Kapoor PN, Klabunde KJ (2001) Reactions of VX, GB, GD, and HD with Nanosize Al_2O_3. Formation of aluminophosphonates. J Am Chem Soc 123:1636–1644

36. Balow RB, Lundin JG, Daniels GC, Gordon WO, Mcentee M, Peterson GW, Wynne JH, Pehrsson PE (2017) Environmental effects on zirconium hydroxide nanoparticles and chemical warfare agent decomposition: implications of atmospheric water and carbon dioxide. ACS Appl Mater Interfaces 9:39747–39757